

# Journal of Geophysical Research: Solid Earth

## RESEARCH ARTICLE

10.1002/2017JB014203

### Key Points:

- A new 3-D  $V_s$  model for NE Tibet and western Northern China Craton is constructed
- Multiple processes contributed to the crustal deformation in NE Tibet
- Western Alxa block and southwestern Ordos block have been modified

### Supporting Information:

- Supporting Information S1
- Table S1
- Table S2

### Correspondence to:

X. Wang and Z. Ding,  
wangxingchen123@sina.com;  
zhfdng@vip.sina.com

### Citation:

Wang, X., Y. Li, Z. Ding, L. Zhu, C. Wang, X. Bao, and Y. Wu (2017), Three-dimensional lithospheric  $S$  wave velocity model of the NE Tibetan Plateau and western North China Craton, *J. Geophys. Res. Solid Earth*, 122, 6703–6720, doi:10.1002/2017JB014203.

Received 13 MAR 2017

Accepted 12 AUG 2017

Accepted article online 17 AUG 2017

Published online 31 AUG 2017

## Three-dimensional lithospheric $S$ wave velocity model of the NE Tibetan Plateau and western North China Craton

Xingchen Wang<sup>1,2</sup> , Yonghua Li<sup>1,2</sup>, Zhifeng Ding<sup>1,2</sup>, Lupei Zhu<sup>3</sup>, Chunyong Wang<sup>1</sup>, Xuwei Bao<sup>4</sup>, and Yan Wu<sup>1,2</sup>

<sup>1</sup>Institute of Geophysics, China Earthquake Administration, Beijing, China, <sup>2</sup>Key Laboratory of Seismic Observation and Geophysical Imaging, China Earthquake Administration, Beijing, China, <sup>3</sup>Department of Earth and Atmospheric Sciences, Saint Louis University, St. Louis, Missouri, USA, <sup>4</sup>School of Earth Sciences, Zhejiang University, Hangzhou, China

**Abstract** We present a new 3-D lithospheric  $V_s$  model for the NE Tibetan Plateau (NETP) and the western North China Craton (NCC). First, high-frequency receiver functions (RFs) were inverted using the neighborhood algorithm to estimate the sedimentary structure beneath each station. Then a 3D  $V_s$  model with unprecedented resolution was constructed by jointly inverting RFs and Rayleigh wave dispersions. A low-velocity sedimentary layer with thicknesses varying from 2 to 10 km is present in the Yinchuan-Hetao graben, Ordos block, and western Alxa block. Velocities from the middle-lower crust to the uppermost mantle are generally high in the Ordos block and low in the Alxa block, indicating that the Alxa block is not part of the NCC. The thickened crust in southwestern Ordos block and western Alxa block suggests that they have been modified. Two crustal low-velocity zones (LVZs) were detected beneath the Kunlun Fault (KF) zone and western Qilian Terrane (QLT). The origin of the LVZ beneath the KF zone may be the combined effect of shear heating, localized asthenosphere upwelling, and crustal radioactivity. The LVZ in the western QLT, representing an early stage of the LVZ that has developed in the KF zone, acts as a decollement to decouple the deformation between the upper and lower crust and plays a key role in seismogenesis. We propose that the crustal deformation beneath the NETP is accommodated by a combination of shear motion, thickening of the upper-middle crust, and removal of lower crust.

## 1. Introduction

The NE Tibetan Plateau (NETP) is one of the best places to study continental crustal deformation on Earth. This region is composed of a series of NW-SE trending terranes, including the Songpan-Ganzi Terrane (SGT), the Western Qinling Terrane (WQT), and the Qilian Terrane (QLT). These terranes are separated by several major active thrust and strike-slip faults, i.e., the Kunlun fault (KF), the Qinling Fault, the Haiyuan Fault (HF), and the North Qilian Fault (NQF) (Figure 1). The tectonics of this region is closely related to the India-Asia collision that began at approximately 50 Ma [Yin and Harrison, 2000]. The continent-continent collision has resulted in significant thickening of the crust.

Many previous studies focused on the mechanisms of crustal thickening in the Tibetan Plateau (TP). Those studies proposed a number of models to explain the tectonic evolution and rapid uplift of the Tibetan Plateau. Among them, three models have received the most attention: rigid block extrusion [Tapponnier and Molnar, 1976; Tapponnier et al., 1982], continuous deformation of the entire lithosphere [England and McKenzie, 1982; England and Houseman, 1986], and channel flow in the lower crust [Clark and Royden, 2000; Royden et al., 1997]. Tomography studies [e.g., Bao et al., 2013; Cheng et al., 2016; Jiang et al., 2014; Li et al., 2013, 2014, 2016; Yang et al., 2012; Zhang et al., 2011; Zheng et al., 2016] and active-source seismic profiling [e.g., Liu et al., 2006; Zhang et al., 2013] revealed low-velocity zones (LVZs) in the crust beneath NETP, which seemed to support the channel flow model. However, the extent and magnitude of the LVZs beneath NETP are still poorly constrained, because the previous tomographic results have a limited spatial resolution. Furthermore, seismic anisotropy results obtained by shear wave splitting measurements indicate that NETP exhibits a vertically coherent deformation in the lithosphere [e.g., Flesch et al., 2005; Li et al., 2011; Wang et al., 2008, 2016], which is inconsistent with the channel flow model. In addition, receiver function studies showed low Poisson's ratios in NETP [Li et al., 2006; Pan and Niu, 2011; Tian and Zhang, 2013; Vergne et al., 2002; Wang et al., 2016; X. Wang et al., 2017; W. Wang et al., 2017] that suggest that the crustal thickening

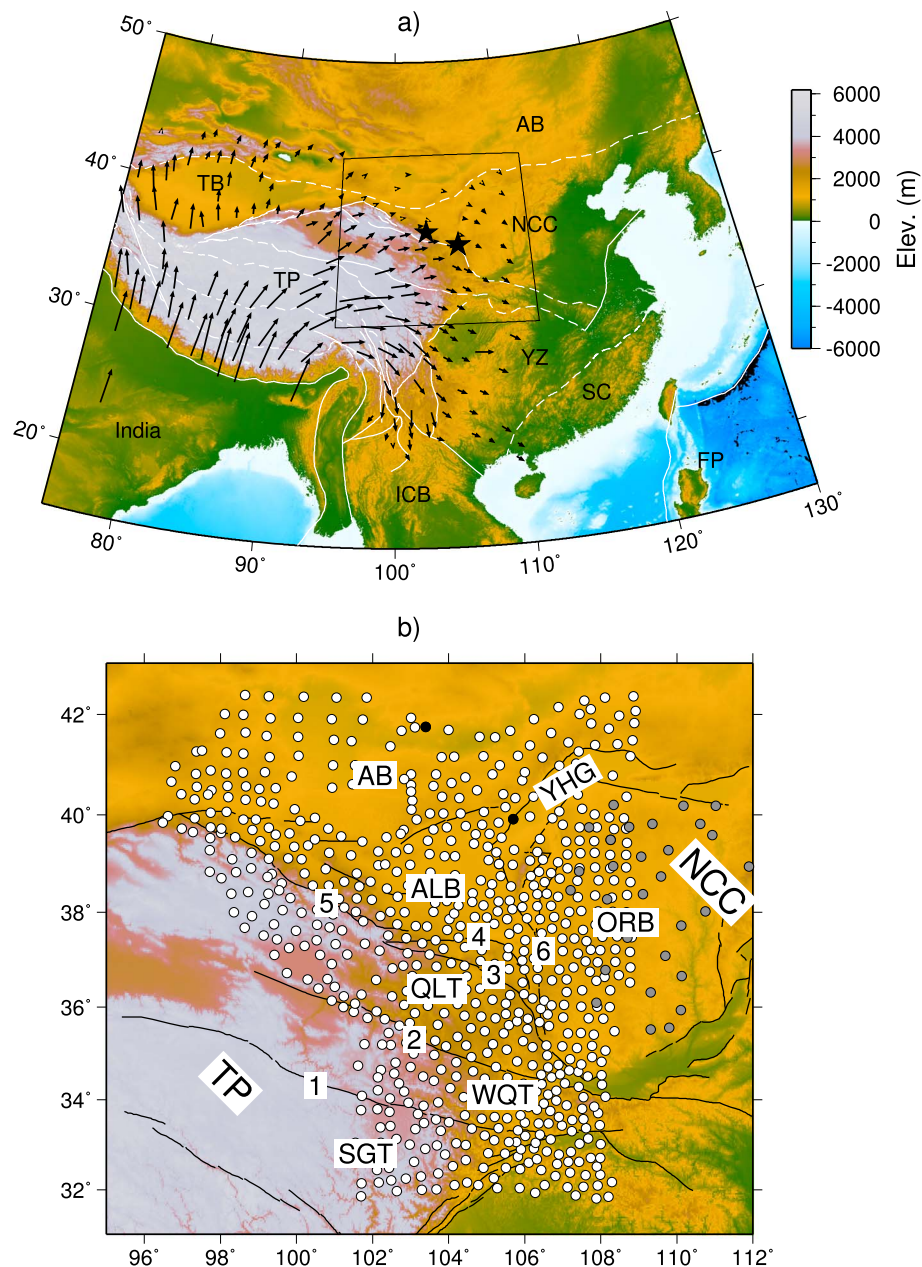


**Figure 1.** (a) Topography of China and neighboring regions. White lines denote sutures and block boundaries. AB: Amurian Block; NCC: North China Craton; TB: Tarim Block; TP: Tibetan Plateau; YZ: Yangtze Block; SC: South China Block; IC: Indo-China Block. The box marks the study area. Black arrows represent GPS velocity field relative to the India Plate [Gan et al., 2007]. Black stars represent the Gulang and Haiyan earthquakes. (b) Major tectonic units in the study region. White and gray dots represent the locations of 673 broadband seismic stations of ChinArray (Phase II) and 51 temporary stations [H. Wang et al., 2014]. Two stations (15585 and 15596) are highlighted by black dots. Black lines are major faults. 1: Kunlun Fault (KF); 2: Qingling Fault (QF); 3: Haiyuan Fault (HF); 4: Xiangshan-Tianjingshan Fault (XTF); 5: North Qilian Fault (NQF); 6: Liupanshan Thrust. ALB: Alxa block; ORB: Ordos block; QLT: Qilian Terrane; WQT: Western Qingling Terrane; SGT: Songpan-Ganzi Terrane; YHG: Yinchuan-Hetao Graben.

of NETP is predominantly caused by upper crustal shortening [Li et al., 2006; Tian and Zhang, 2013; Vergne et al., 2002] or vertically coherent shortening [Pan and Niu, 2011; Wang et al., 2016].

The Alxa block and the Ordos block, which are traditionally considered to be parts of the western North China Craton (NCC), have resisted the northeastward expansion of the Tibetan Plateau [Chang et al., 2011; Shen

*et al.*, 2017]. Whether or not these two blocks have been modified is a subject of debate. The thick lithosphere of the Ordos block indicates that it has preserved a cratonic keel [Chen, 2010; Chen *et al.*, 2014; Wang *et al.*, 2013; Shen *et al.*, 2017; Zhang *et al.*, 2012]; however, results of shear wave splitting suggest that the thick lithospheric root of the southwestern Ordos block is currently being replaced with hot Tibetan asthenosphere [e.g., Yu and Chen, 2016]. In addition, it is currently uncertain whether the Alxa block is part of the NCC. Evidence from zircon U-Pb geochronology suggested that the Alxa block was most likely an integrated component of the western NCC [e.g., Gong *et al.*, 2015]; however, recent geological studies suggested that the Alxa block is not a part of the NCC [e.g., Dan *et al.*, 2016]. Detailed lithospheric structure can constitute an important source of information for understanding the geological evolution of the western NCC. However, the sparsely distributed seismic stations are not sufficient to elucidate the detailed lateral variations in the lithospheric structure beneath the Alxa block. Therefore, it is imperative to carry out a high-resolution study of lithospheric velocity structural features to understand the tectonic processes in NETP and western NCC.

In addition to significant crustal thickening, the NETP is characterized by the highest level of seismicity in the mainland China. This region has experienced several earthquakes of  $M_s \geq 8.0$  in the past, such as the 1920 Haiyuan  $M_s$  8.5 and the 1927 Gulang  $M_s$  8.0 earthquakes (Figure 1). However, the mechanism for the occurrence of the earthquakes remains unclear. Further understanding of the seismotectonics also requires seismological constraints on the crustal structure at a high spatial resolution.

In this study, we obtained a new 3-D S wave velocity model of the crust and uppermost mantle in the NETP and western NCC by joint inversion of *P* wave receiver functions (RFs) and Rayleigh wave dispersion. The resulting images can provide important insights into the mechanism of crustal deformation and tectonic processes in this region.

## 2. Data

RFs were obtained from teleseismic *P* waveforms recorded at 724 seismic stations in the NETP and surrounding regions (Figure 1). The stations include 673 broadband stations in a temporary seismic network of ChinArray (Phase II) [ChinArray-Himalaya, 2011] that was deployed during the period from September 2013 to April 2016 and 51 broadband stations belonging to a temporary network deployed in the Ordos block between April 2010 and December 2011. The average interstation distance was ~40 km. Each station consisted of a Guralp CMG-3ESP or CMG-3ESP seismometer and a Reftek 130 data acquisition system. The two arrays provided a good opportunity to reveal detailed lithospheric structure in the study region.

Rayleigh wave phase velocities at periods of 10–80 s and group velocities at periods of 10–70 s from a surface wave tomographic study of Li *et al.* [2017] were used for a joint inversion with receiver function of 698 stations located in the area covered by the ChinArray (Phase II). In that study, interstation phase and group velocities of Rayleigh waves were measured based on analysis of teleseismic waveform data recorded by 673 seismic stations from the ChinArray (Phase II). These dispersions were then used tomographically to construct 2-D phase and group velocity maps on a  $0.5^\circ \times 0.5^\circ$  grid covering the western part of the study region. Checkerboard resolution tests showed that the horizontal resolution was approximately  $0.5^\circ$  for the periods used in this study.

For the 26 remaining stations, the Rayleigh wave phase and group velocities used were extracted from the tomographic results of Bao *et al.* [2015a]. That work was a large-scale study of surface wave tomography across mainland China, in which group and phase velocities within the 10–140 s period range were obtained from ambient noise and earthquake data recorded by more than 1300 permanent and portable broadband stations. The combined data sets were used to form tomographic phase and group velocity maps of  $0.5^\circ \times 0.5^\circ$  cells. The resolution was approximately  $1\text{--}2^\circ$  in our study area.

## 3. Method

### 3.1. Calculation of *P* Wave RFs

*P* wave RFs were computed using seismograms from 1120 teleseismic events with good signal-to-noise ratios, magnitudes greater than  $M_s$  5.5, and epicentral distances between  $30^\circ$  and  $90^\circ$  during the operation period of these stations (Figure 2). All the waveforms have clear *P* arrivals. These earthquakes present reasonably good back azimuth coverage that could reduce influence from lateral crustal structural

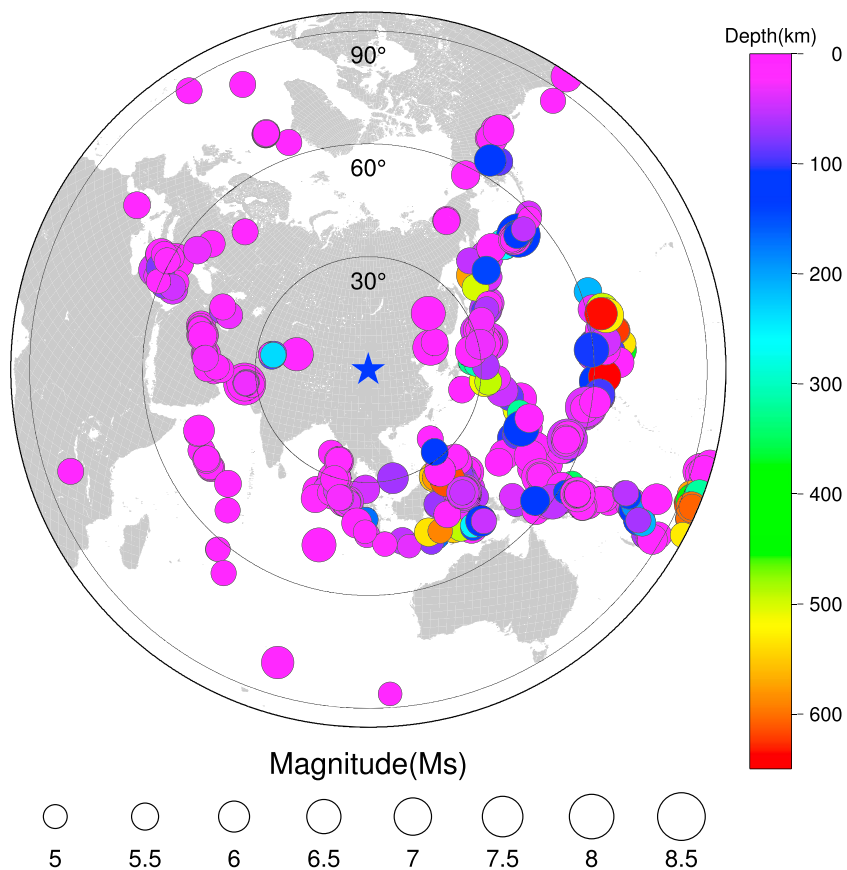


**Figure 2.** Distribution of the teleseismic events used to calculate the receiver function. Blue star denotes the center of the study area. The event locations are given by circles whose sizes are proportional to event magnitude ( $M_s$ ) and are color coded by focal depths. Three epicentral distances of 30°, 60°, and 90° from the center of the study area are also shown.

variations on the results. We first preprocessed the waveform data by decimating to 10 samples per second and band-pass filtering them from 0.02 to 1 Hz. To generate RFs, we further rotated two horizontal-component seismograms into the radial ( $R$ ) and transverse ( $T$ ) components. The  $R$  and  $T$  components were deconvolved from the vertical component to obtain RFs using a time-domain deconvolution method [Ligorra and Ammon, 1999]. To remove high-frequency noise, we used a Gaussian low-pass filter with a Gaussian parameter of 2.0. We visually inspected all the RFs and removed those without a clear first  $P$  arrival phase. After careful inspection, the number of RFs selected at these stations varies from 50 to 363, with a total of 100,493 RFs. RFs of two representative stations are shown in Figure 3. The RFs of station 15585 show clear Moho  $P_s$  phases (Figure 3). The direct  $P$  arrivals of RFs at station 15596, which was located in the Yinchuan-Hetao (YH) graben, appear clearly shifted from zero, due to the presence of thick sediments at shallower depths. Additional examples are provided in Figures S1 and S2 in the supporting information.

### 3.2. Determination of Sedimentary Structure

As mentioned above, there are thick sediments in the YH graben and northern Ordos block. As thick sedimentary basins have rather low seismic velocity and density values, erroneous structure of the sedimentary cover can be mapped into deep crustal structure. Hence, accurate knowledge of the sedimentary layer in the starting model should be considered in the joint inversion. The sedimentary layer structure beneath each station was obtained by inversion of higher-frequency RFs (Gaussian filter parameters  $\alpha = 5.0$ ) using the neighborhood algorithm (NA) method [Sambridge, 1999].

Details of the model space searched by NA are provided in Table 1. The model is described by four parameters for each layer: the thickness, the shear wave velocities at the top and at the bottom point of the

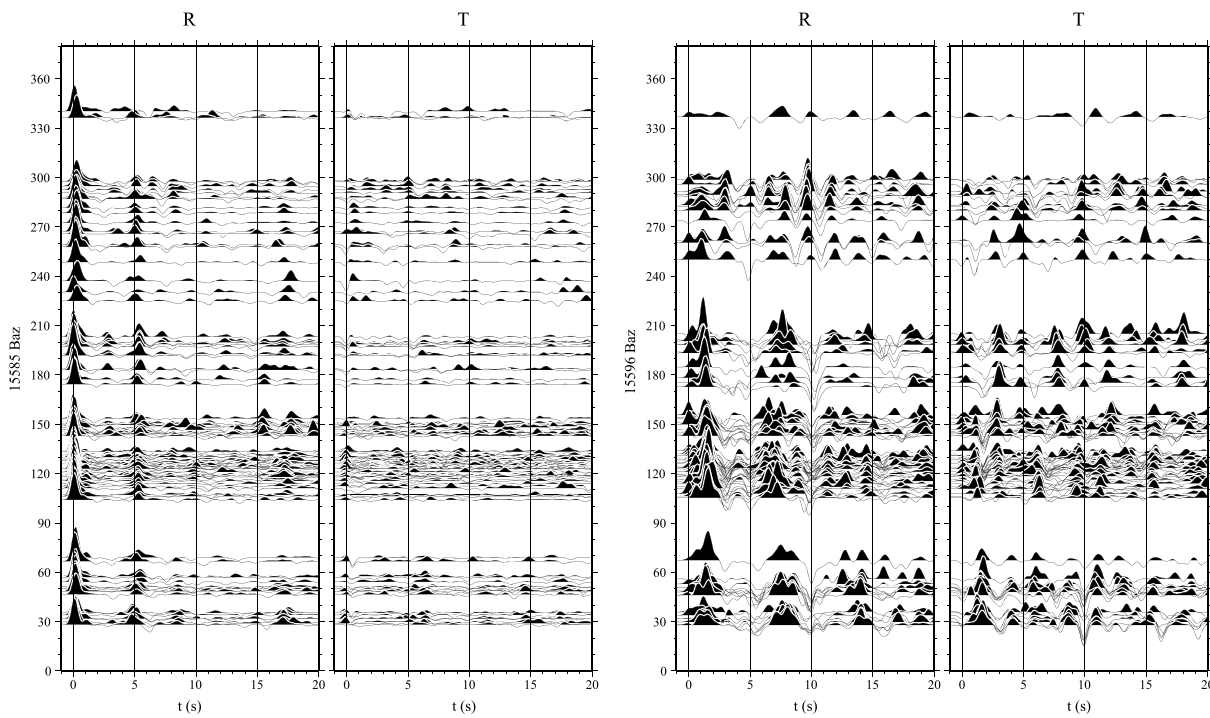


**Figure 3.** Radial and transverse components of RFs as a function of back azimuth at stations (left) 15585 in the Amurian block and (right) 15596 in the Yinchuan-Hetao graben (Figure 1). R and T denote the radial and transverse components, respectively.

layer, and the  $V_p/V_s$  ratio. We stacked RFs of similar ray parameters (within 0.01 s/km) and azimuths (piercing points at 40 km depth within 1 km). We performed the NA processes described by Srinivas *et al.* [2013] using the 5 s of the stacked radial RFs. The structure of the sedimentary layers beneath each station was obtained from the best 1000 models of least misfit at the station (Figure 4).

### 3.3. Joint Inversion of RFs and Rayleigh Wave Dispersions

Shear wave velocity model of each station was obtained by jointly inverting the RFs with Rayleigh wave phase and group velocities, which has been confirmed to be an effective method [e.g., Julià *et al.*, 2000, 2005; Bao *et al.*, 2015b; Zheng *et al.*, 2016]. The joint analysis of RFs and Rayleigh wave phase and group velocities provides tighter constraints on the S wave velocity structure than using them separately [e.g., Bao *et al.*, 2015b; Zheng *et al.*, 2016]. Here we used an iterative damped least squares technique to invert for the lithospheric  $V_s$  structure in the NETP and western NCC [Herrmann, 2013; Julià *et al.*, 2000].

Variations of RFs from different azimuths are apparent at some stations (Figure S1), which may be related to the presence of anisotropy and/or dipping layers. However, these differences are quite small and the Moho  $P_s$  phases are generally identical for different azimuths. Stacked RFs were also used in the joint inversion; thus, the structure obtained by RF inversion reflects the laterally averaged tectonic characteristics beneath the station. The Rayleigh wave dispersion curves of each station were extracted from the corresponding tomographic grids maps.

**Table 1.** Model Spaces Searched by the NA Approach

	Thickness (km)	$V_s$ at the Topmost Point (km/s)	$V_s$ at the Bottommost Point (km/s)	$V_p/V_s$
Sediment Layer	0.1–10.0	0.1–1.5	1.0–3.0	2.0–3.0
Upper crust	10.0–40.0	3.0–4.0	3.0–5.0	1.6–2.0

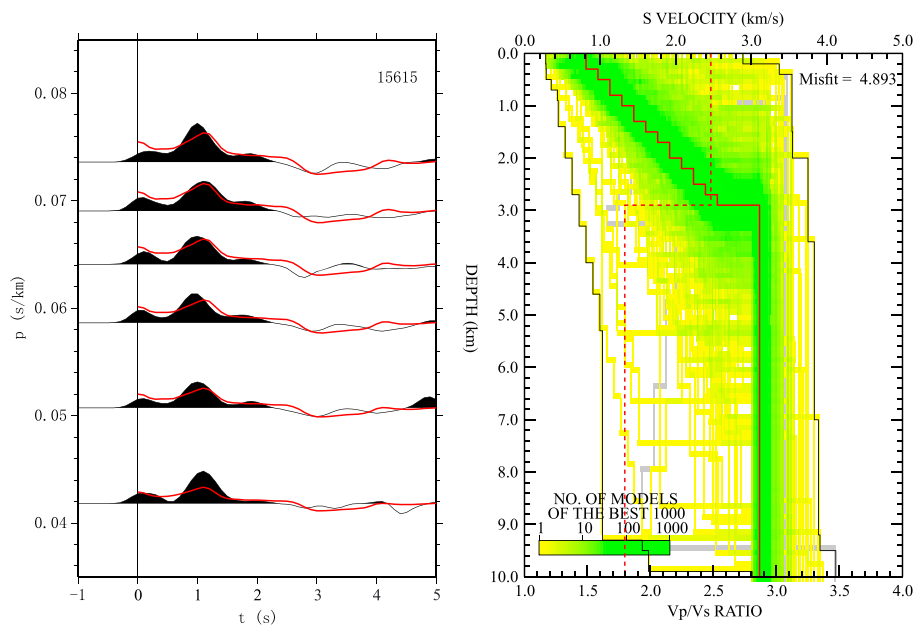


**Figure 4.** Example of NA determination of the sedimentary structure at stations 15615. (left) Black and red lines represent observed and predicted RFs, respectively. (right) Yellow and green lines represent the best 1000 models. Red solid and red dashed lines represent the preferred model and the  $V_p/V_s$  ratio, respectively.

The starting model for each station was constructed using the velocity model in the top 10 km (from the results of NA), then, gradually increasing the  $S$  wave velocity to 4.57 km/s at 0.1 km/s per 2 km and connecting to the velocity of the IASPEI91 model down to 100 km depth. The  $V_p/V_s$  ratio in the crust was set according to the RF  $H\text{-}\kappa$  stacking results [W. Wang *et al.*, 2017], and the  $V_p/V_s$  ratio in the mantle was set to 1.80. Crustal densities were computed from the  $P$  wave velocities using the empirical relationship of Berteussen [1977]. The layer thickness is 0.4 km in the top 2 km of the model, 1 km between 2 and 4 km depth, and 2 km from 4 to 100 km depth.

The relative weight  $p$  of the RF and dispersion data is an important parameter in the joint inversion. To demonstrate the stability of our inversion scheme and estimate the uncertainties of the resulting models, we repeatedly performed the inversions using a range of  $p$  values from 0.1 to 1.0. Finally, the weight was set to 0.5 to obtain a relatively fine  $S$  wave velocity model. The tests demonstrated that the uncertainties of the shear wave velocity in each layer were less than 0.05 km/s (Figure S3).

We also used a simple initial model with a constant shear wave velocity of 4.6 km/s, a  $V_p/V_s$  ratio of 1.75, and a density of 3.3 kg/m<sup>3</sup> from the surface down to 100 km depth to evaluate the error of our velocity model [e.g., Zheng *et al.*, 2016]. The joint inversion results for representative stations 63018 and 63041 are displayed in Figure 5. The tests demonstrated the stability of our method and showed that an initial velocity model that included the sedimentary shear wave velocity was better in resolving the seismic structure beneath a station sitting on unconsolidated sediments.

In addition, synthetic tests were performed to evaluate the robustness of our model. Synthetic RFs and Rayleigh wave phase and group velocities generated by the resulting models were used as real data. We performed joint inversion of synthetic data using the same scheme as for the real data. The tests demonstrated that the velocity models were well recovered, confirming the robustness of our method (Figure S4).

Because an east-west structural variation in the Ordos block, if present, could be an artifact of using two different seismic networks and tomographic models, we also compared the joint inversion results for stations 15724 and B031, belonging to the two networks but close in location in the western Ordos block. The comparison showed a good agreement with each other (Figure S5). Therefore, we believe that the two data sets can be jointly used to construct 3-D lithospheric structure beneath the Ordos block.

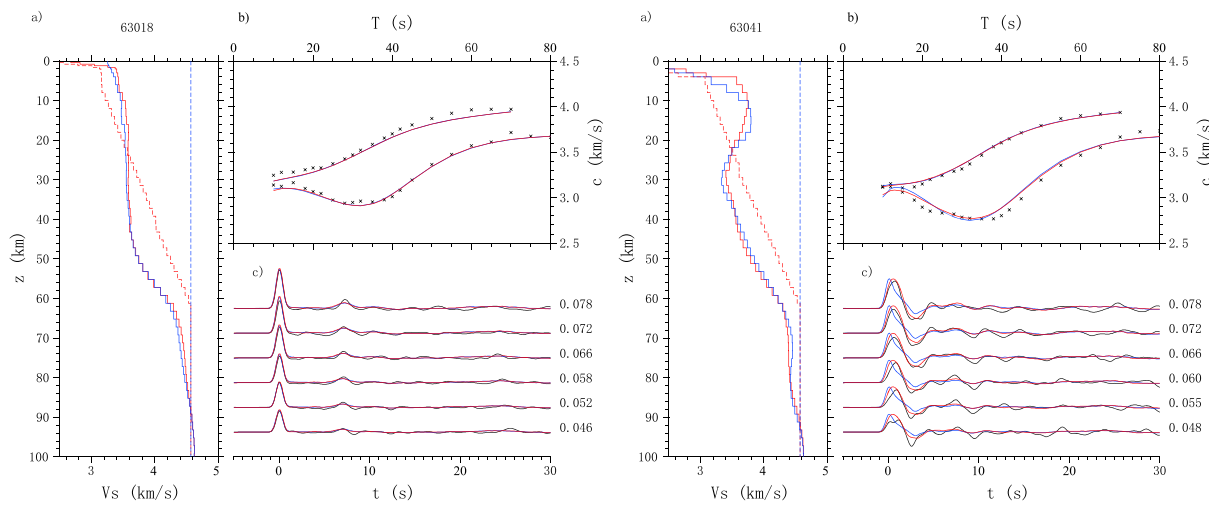


**Figure 5.** Examples of the joint inversion for stations (left) 63018 and (right) 63041. (a) The final model (red line) generated by a starting model with a sedimentary layer (red dashed line) and final model (blue line) generated by a constant starting model (blue dashed line). (b) Observed phase and group velocities (black crosses) and predictions of the final model from the sedimentary layer starting model (red lines) and from the constant starting model (blue lines). (c) Observed RFs (black line) and predicted RFs of the final model from the sedimentary layer starting model (red line) and from the constant starting model (blue line). Ray parameters are indicated to the right of the waveforms.

## 4. Results

### 4.1. Sediment Thickness

Our results reveal detailed depositional characteristics of sediments in NETP and western NCC (Figure 6). Thick sedimentary layer is detected in the YH graben and western Alxa block, whereas the eastern Ordos block is characterized by a thin sedimentary layer. The maximum sedimentary thickness of the YH graben is about 10 km. The sedimentary thickness in the Ordos block decreases from 5–6 km in the west to 3–4 km in the east, with an average thickness of ~4 km.

Our findings are consistent with results of active-source seismic profiling in the YH graben and Ordos block [e.g., Guo *et al.*, 2016; Feng *et al.*, 2011; Nie *et al.*, 2011; C. Y. Wang *et al.*, 2014; Teng *et al.*, 2014]. The sedimentary thickness estimated in this study and from the Crust1.0 model exhibits significant differences. Sedimentary layer that exists in the Crust1.0 model revealed depositional characteristics only for the Ordos block, but not for the YH graben and Alxa block. There are also slight differences between the sedimentary

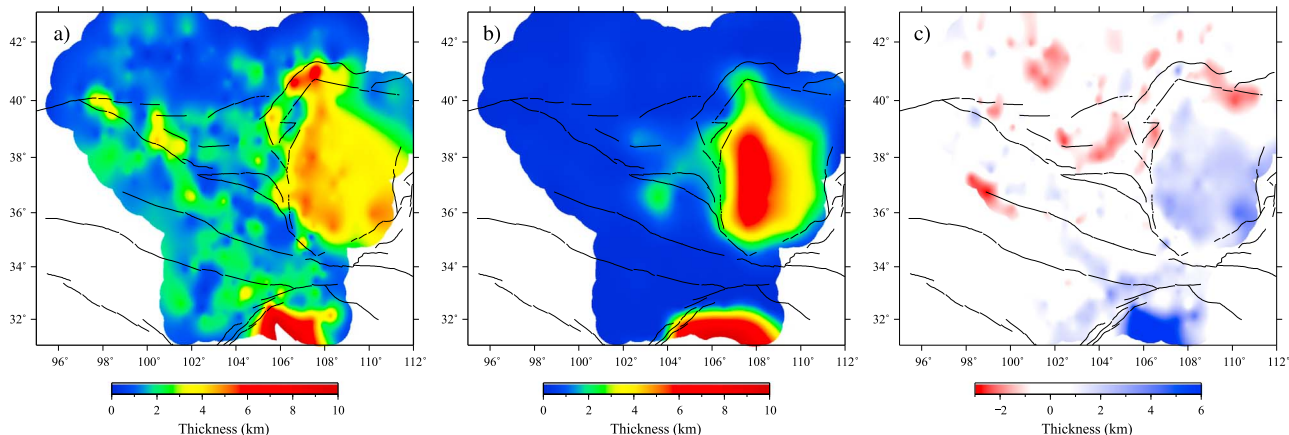


**Figure 6.** (a) Sedimentary thickness estimated using the NA approach. (b) The Crust1.0 model. (c) The differences between the sedimentary thicknesses in this study and those from X. Wang *et al.* [2017].

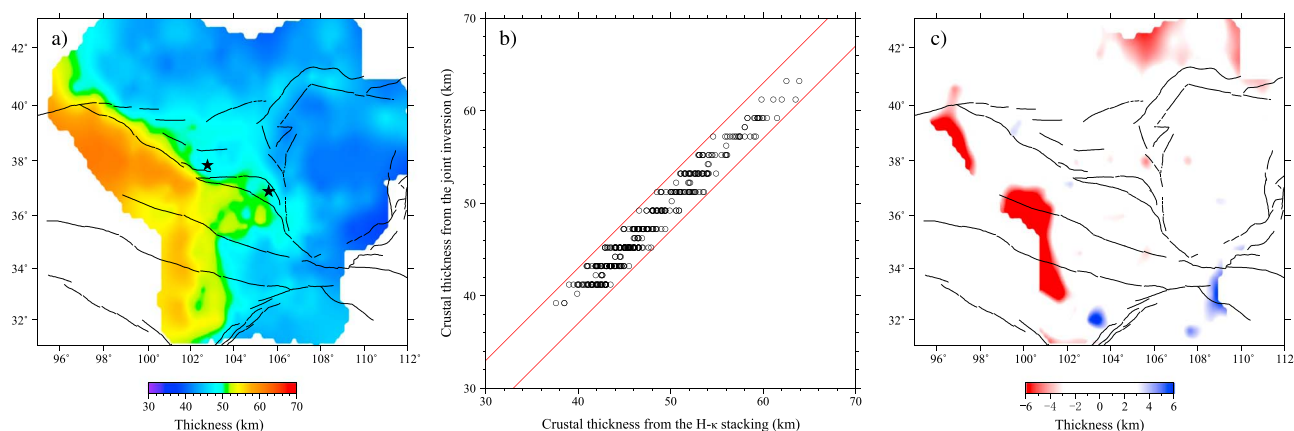


**Figure 7.** (a) Estimated crustal thickness from the joint inversion. Black stars indicate earthquakes with magnitude ( $M_s$ )  $\geq 8.0$ . (b) Comparison of crustal thickness determined from the  $H\text{-}\kappa$  stacking method [H. Wang et al., 2014; W. Wang et al., 2017] with from the joint inversion method. Black lines indicate  $\pm 3$  km deviation. (c) The difference between the crustal thicknesses estimated from the joint inversion and from the active-source seismic profiling [Teng et al., 2013].

thickness estimated in this study and by X. Wang et al. [2017]. The sedimentary thickness in the YH graben and western Ordos block estimated in this study is 2–3 km thicker than the values of X. Wang et al. [2017] that were estimated by the relationship between the sedimentary thicknesses and the delay times, which represents the thickness of the unconsolidated sediment layer.

#### 4.2. Crustal Thickness

The depth at which the vertical velocity gradient reaches a local maximum in the velocity range 3.8–4.3 km/s is regarded as the Moho [e.g., Bao et al., 2015b]. The estimated crustal thicknesses were further interpolated into meshed  $0.2^\circ \times 0.2^\circ$  grids of the study area (Figure 7a). The crustal thickness varies from ~65 km in the NETP to ~40 km in the western NCC (Figure 7), which is consistent with previous estimates from the  $H\text{-}\kappa$  stacking method [e.g., Li et al., 2006, 2014, 2015; Pan and Niu, 2011; Tian and Zhang, 2013; H. Wang et al., 2014; Wang et al., 2016; X. Wang et al., 2017; W. Wang et al., 2017; Xu et al., 2014; Zheng et al., 2016] and active-source seismic profiles [e.g., Jia et al., 2010; Liu et al., 2006; Teng et al., 2013; C. Y. Wang et al., 2014; S. J. Wang et al., 2014]. A difference in the Moho depth is observed from the QLT to Alxa block by as much as 10 km across the HF and NQF (Figure 7). In addition to the significant contrast in crustal thickness between the QLT and Alxa block, the crustal thickness also exhibits significant lateral variation within each block (Figure 7). There is a remarkable contrast between the western and eastern Alxa block: the western Alxa block features a thick crust (~50 km), whereas the eastern Alxa block has a thin crust (~45 km). The crust is relatively thick (~65 km) beneath the western QLT; in contrast, the crust is thin (~50 km) beneath the eastern QLT. The crustal thickness in the WQT decreases from ~60 km in the west to ~40 km in the east.

Comparison between the crustal thicknesses estimated by the joint inversion and those obtained using the  $H\text{-}\kappa$  stacking method [W. Wang et al., 2017] reveals that the differences are less than 3 km for all stations (Figure 7b). Figure 7c shows that our measurements of crustal thicknesses also coincide with those determined from active-source seismic profiling [Teng et al., 2013]. The differences are less than 3 km for most areas except the southwestern margin of the study region where active-source seismic profiles are scarce.

#### 4.3. Three-Dimensional S Wave Velocity Model

A 3-D S wave velocity model of the crust and upper mantle with a lateral resolution of approximately 40 km beneath the NETP and western NCC was obtained by combining the joint inversion results of 708 stations. S wave velocity maps at depths of 2, 12, 24, 36, 50, 66, 82, and 98 km are shown in Figure 8, and five representative cross sections are displayed in Figure 9. These images show different features of velocities at different depths.

At the shallow depth (Figure 8a), obvious low- $V_s$  anomalies are present in the YH graben and Ordos block, reflecting the thick widespread Tertiary sediments and Quaternary loess. The YH graben is characterized

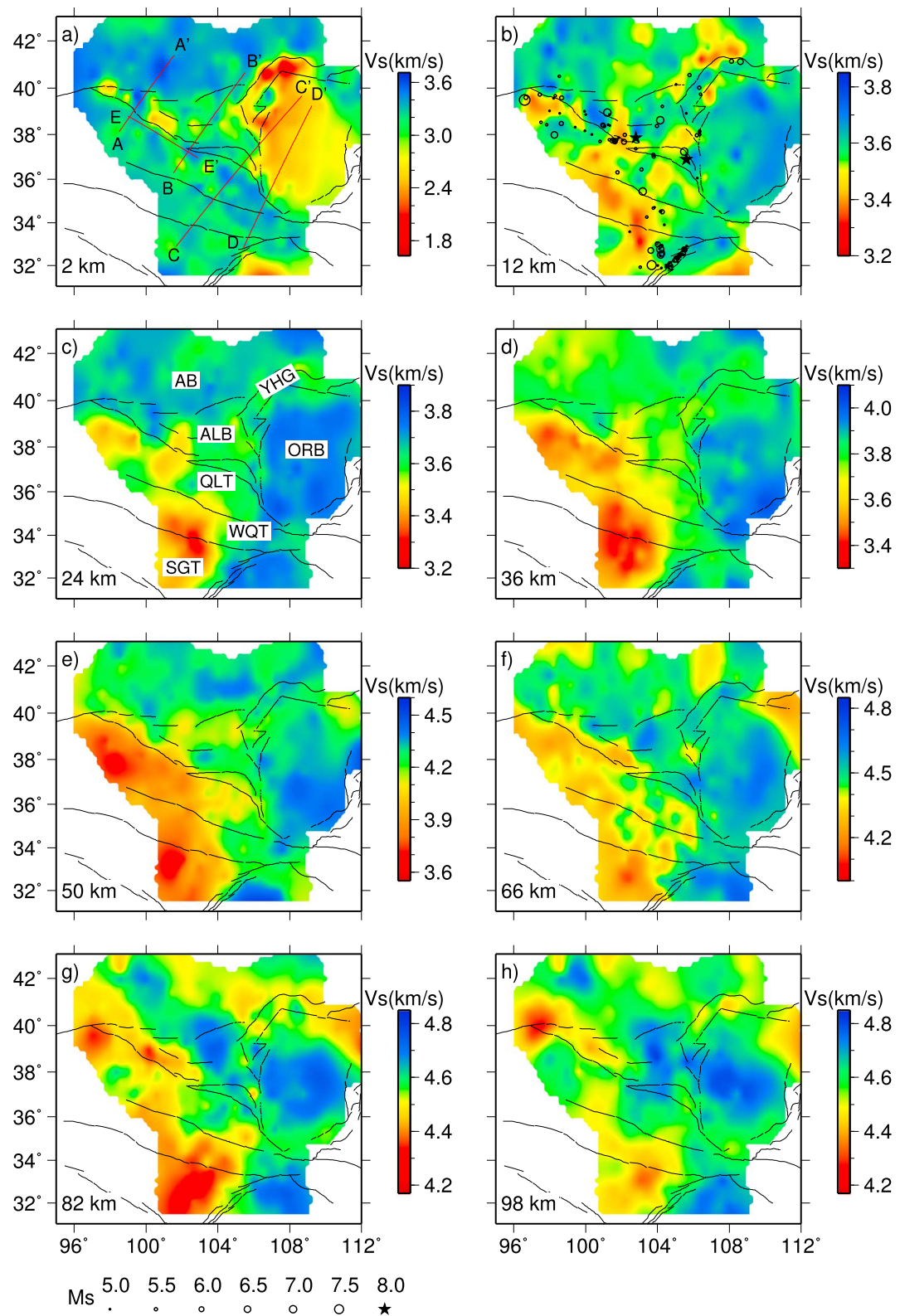


**Figure 8.**  $V_s$  at depths of 2, 12, 24, 36, 50, 66, 82, and 98 km. Red lines AA'-EE' in Figure 8a indicate the locations of the velocity cross sections in Figure 9. The seismicity (1900–2016) is shown in Figure 8b. Abbreviations in Figure 8c are detailed in Figure 1.

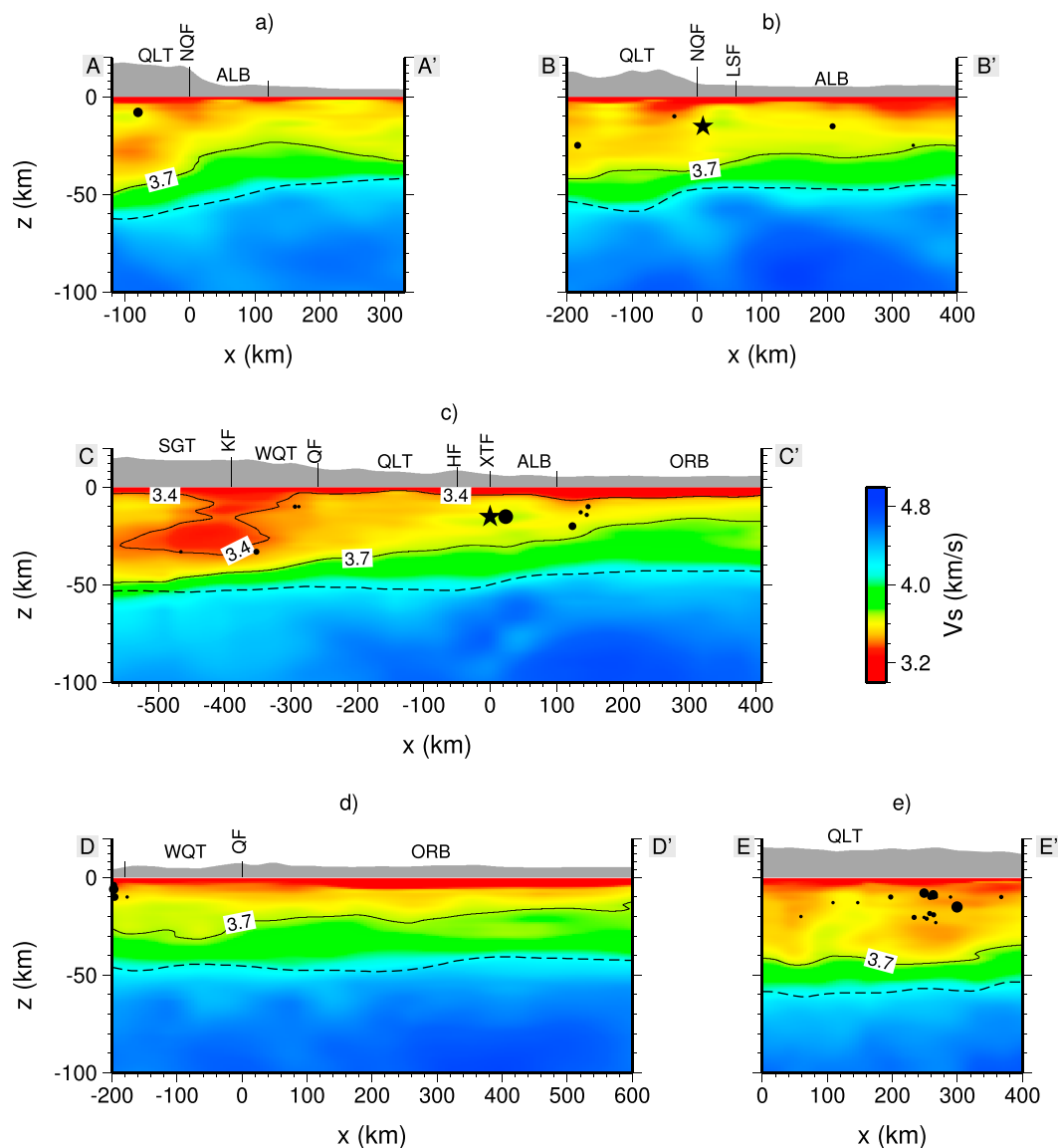


**Figure 9.** Vertical cross sections of  $V_s$  along the five profiles marked in Figure 8. The surface topography is amplified by a factor of 3. The dashed lines indicate the Moho depth estimated from  $H\text{-}\kappa$  stacking analysis [W. Wang et al., 2017]. The low crustal shear wave speeds in the KF zone ( $<3.4$  km/s) encircled with black contours suggest existence of crustal partial melting. The black contour (3.7 km/s) represents the boundary of the upper-middle crust and lower crust. The stars and dots denote earthquakes with magnitude  $\geq 8.0$  and  $< 8.0$ , respectively. Other labels are explained in the caption of Figure 1.

by the lowest velocity. The velocity within the Ordos block is lower in the northwest and higher in the southeast, indicating that the sedimentary thickness in the Ordos block decreases to the southeast. In the upper crust (Figure 8b), the velocity pattern is characterized by alternating low-velocity anomalies and high-velocity anomalies with the moderate-to-large earthquakes mostly occur in between.

Outside the NETP at the middle-lower crust and uppermost mantle depths of 24, 36, and 50 km (Figures 8c–8e), the  $S$  wave velocities are generally low in the Alxa block, in obvious contrast to the high velocity in the Ordos block. At 66 km depth, which is in the upper mantle outside NETP, the velocity pattern changes. The Ordos block and Alxa block both exhibit high velocities. At depths of 82 and 98 km outside the NETP, the eastern Alxa block and the central part of the Ordos block are characterized by high velocities, whereas low  $S$  wave velocities are present in the western Alxa block and on the periphery of the Ordos block.

Within the NETP at the upper-middle crust depth of 24 km (Figure 8c), which is in the upper-middle crust (Figure 7), the principal feature is a prominent low-velocity anomaly in the northern SGT and western WQT. In addition, Figure 8c also shows low-velocity anomalies clearly beneath the central QLT and western QLT. At depths of 36, 50, and 66 km within the NETP, in the middle-lower crust and uppermost mantle, S wave speeds are generally slower compared to the speeds in the surrounding regions (Figures 8d–f). Two prominent LVZs are revealed in the western QLT, northern SGT, and southwestern WQT in the middle crust (Figures 8c and 8d), which appear particularly clearly in the velocity profiles A-A' in western QLT and C-C' in northern SGT and southwestern WQT (Figure 9). However, at 50–66 km depth the apparent low velocities within the NETP compared to in the surrounding areas are caused by high mantle velocity in the latter at this depth range. At depths of 82 and 98 km within the NETP, the northern SGT and southwestern WQT also feature low-velocity anomalies. However, the low-velocity anomaly beneath the western QLT appears to be shifted northward to span the QLT and Alxa block at 82 km depth and intermediate S wave speeds are present in the western QLT at 98 km depth. In addition, the velocities increase with depth beneath the midcrustal LVZs in the western QLT (Figure 9a).

These general features agree well with previous studies [e.g., *Bao et al.*, 2013; *Cheng et al.*, 2016; *Jiang et al.*, 2014; *Li et al.*, 2013, 2014, 2016; *Yang et al.*, 2012; *Zhang et al.*, 2011; *Zheng et al.*, 2016]. For example, the LVZs in the northern SGT, southwestern WQT, and western QLT were also revealed by the surface wave tomography studies [*Bao et al.*, 2013; *Jiang et al.*, 2014; *Li et al.*, 2014, 2016], but at lower resolution. The crustal LVZ that underlies the western QLT is not as pronounced as that in the SGT [*Bao et al.*, 2013].

## 5. Discussion

We obtained a new 3-D S wave velocity model of the crust and upper mantle with unprecedented clarity for the NETP and western NCC by jointly inverting RFs with Rayleigh wave phase and group velocities. This model can provide important insights into the geodynamic processes in this region. In particular, we discuss four important and yet controversial issues: (1) origin of two crustal LVZs in the northern SGT, southwestern WQT, and western QLT; (2) crustal deformation in the NETP; (3) tectonic processes of the western NCC; and (4) implications for seismogenesis.

### 5.1. Origin of Two Crustal LVZs in the Northern SGT, Southwestern WQT, and Western QLT

Recent seismic tomographic images [e.g., *Bao et al.*, 2013; *Cheng et al.*, 2016; *Jiang et al.*, 2014; *Li et al.*, 2013, 2014, 2016; *Yang et al.*, 2012; *Zhang et al.*, 2011; *Zheng et al.*, 2016] revealed low-velocity anomalies in the crust and upper mantle beneath the NETP. Our model reveals lateral velocity variations in this area with unprecedented resolution. The shear wave velocities in the upper and middle crust within the northern SGT and southwestern WQT (Figures 8c and 8d and Figure 9c) are less than 3.4 km/s, which has been regarded as an indicator of partial melt [*Yang et al.*, 2012]. The relatively high surface heat flow [*Hu et al.*, 2000] and high electrical conductivity [*Zhan et al.*, 2014; *Zhao et al.*, 2015] observed also support the presence of crustal partial melting beneath the northern SGT and southwestern WQT. The localized LVZ in upper and middle crust is located along the strike-slip KF, whose slip rate is 10–12 mm/yr in the western part, suggesting a significant relative movement between the WQT and SGT [e.g., *Gan et al.*, 2007]. Thus, the coincidence of the KF zone and LVZ revealed here implies a close relationship between LVZ and the shear heating resulted from the relative movement across the fault [*Leloup et al.*, 1999].

However, the numerical modeling by *Leloup et al.* [1999] showed that the shear heating is limited in a narrow zone that is tens of kilometers wide. Thus, the shear heating alone fails to explain the broad lenticular LVZ in the middle crust beneath the KF, which extends to 150 km south of the KF. *Li et al.* [2013, 2016] suggested that another heat source for the LVZ beneath the KF zone is from asthenosphere upwelling caused by the removal of lithosphere root. The presence of relatively low velocity in upper mantle may account for the mantle flow beneath the WQT [e.g., *Guo and Chen*, 2017; *Li et al.*, 2016, 2017; *Zheng et al.*, 2016]. Shear wave splitting measurements also suggested that the asthenosphere mantle flow existed beneath the WQT [e.g., *Chang et al.*, 2017; *Yu and Chen*, 2016]. The absence of mafic lower crust characterized by high velocity is obvious from our 3-D  $V_s$  model (Figure 9c) and DSS studies [*Vergne et al.*, 2002; *Liu et al.*, 2006], which could be a consequence of removal of mafic lower crust [*Chung et al.*, 2005; *Guo and Chen*, 2016]. Petrological study suggested a granodioritic to quartz-dioritic crustal composition beneath the WQT [e.g., *Gao et al.*, 1992]. Thus, we conclude that the mantle flow beneath the WQT may

have caused the delamination of lower crust beneath the northern SGT and southwestern WQT and subsequent asthenosphere upwelling, similar to what has been inferred for the Canadian Cordillera [e.g., *Bao et al.*, 2014]. The uppermost mantle above 100 km in the KF zone is imaged by a low-velocity anomaly (Figure 9c), which can be interpreted as asthenosphere upwelling.

Additionally, numerical experiments showed that crustal radioactivity can produce heat to cause the temperature to rise and lower the value of  $V_s$  in the crust [Hacker *et al.*, 2000; Harley, 1989, 2004]. The thickening of the crust in the NETP would naturally lead to heating of the middle-lower crust due to crustal radioactivity [e.g., *McKenzie and Priestley*, 2008]. When the crustal temperatures exceed the solidus, melting will occur, and the upward movement of melt will transport the radioactive elements to the upper part of the crust (Figure 10). Thus, another heat source available is crustal radioactivity, which can also be responsible for regional LVZ. Based on our geophysical data and analyses presented here along with previous studies, we suspect that the LVZ beneath the northern SGT and southwestern WQT may be caused by a combined effect of shear heating, localized asthenosphere upwelling, and crustal radioactivity (Figure 10), though further studies are needed to confirm this. Another interesting feature is a local LVZ in the middle crust beneath the western QLT (Figure 9a). Surface motion also demonstrates a significant difference between the QLT and Alxa block across the HF and NQF [e.g., *Gan et al.*, 2007; *Liang et al.*, 2013], indicating obvious relative movement between QLT and Alxa block along NQF. Thus, we speculate that the relative movement between QLT and Alxa block along NQF can also cause the shear heating, which could contribute to reduce crustal velocity and thus the formation of LVZ. The crustal LVZ beneath the western QLT has higher velocities and higher electrical resistivity [e.g., *Xiao et al.*, 2013, 2016] (thus perhaps higher viscosity) compared to the LVZ in the KF zone, which may indicate that the partial melting is not likely to be present in the western QLT. In addition, the western QLT exhibits a thick crust with a low  $V_s$  value in the uppermost mantle (Figure 9a); in contrast, thin crust with a relatively low velocity in the uppermost mantle (Figure 9c) is present beneath the northern SGT and southwestern WQT. Thus, the LVZ in the western QLT may represent an early stage of the LVZ that has developed in the northern SGT and southwestern WQT [*Bao et al.*, 2013; *Li et al.*, 2014].

## 5.2. Crustal Deformation in the NETP

*Clark and Royden* [2000] suggested that the crustal thickening beneath the NETP was due to extrusion of the ductile middle-to-lower crustal rocks from the center into the margin. The crustal LVZs observed by previous tomography studies [e.g., *Cheng et al.*, 2016; *Jiang et al.*, 2014; *Li et al.*, 2014] have been interpreted in support of the crustal channel flow model. However, our observations are incompatible with the crustal channel flow model. The prominent LVZs are mainly present in the upper and middle crust beneath the northern SGT, southwestern WQT, and western QLT (Figures 9a and 9c), appearing as narrow and isolated lenses. No low-velocity layer is imaged in the lower crust within the NETP (Figure 9), indicating that the lower crust with a high viscosity is not conductive to flow. In addition, the moderate-to-high electrical resistivity [e.g., *Xiao et al.*, 2013, 2016], moderate heat flow [e.g., *Hu et al.*, 2000], and low-to-intermediate Poisson's ratios [e.g., *Li et al.*, 2006; *Pan and Niu*, 2011; *Wang et al.*, 2016; *X. Wang et al.*, 2017; *W. Wang et al.*, 2017] further suggest that crustal thickening in the NETP is not produced by the channel flow model.

*England and Houseman* [1986] suggested that the thick crust can be explained by the vertically coherent deformation of the entire lithosphere, which was also inferred from GPS and SKS data [*Wang et al.*, 2008, 2016]. However, our results reveal a positive correlation between the crustal thickness and the thickness of the upper and middle crust ( $V_s < 3.7$  km/s) beneath the NETP (Figures 9a–9c). The upper and middle crust beneath the NETP is marked by a thick low-velocity layer ( $V_s < 3.7$  km/s) compared to the Alxa block and Ordos block with a thin crust, which seems to suggest that the crustal thickening in the NETP is concentrated in the upper-middle crust [*Tian et al.*, 2014; *Zhang et al.*, 2015], inconsistent with the vertically coherent deformation model.

However, this apparent contradiction can be explained by multiple stages of crustal deformation in the NETP. During early plateau growth, the lithospheric rheological condition of the plateau may be similar to the crust-mantle coupled deformation model assumed by *Bendick and Flesch* [2007]. At a late stage, the lower crust delaminated, which induced localized asthenosphere upwelling. At the latest stage, the shear heating and localized asthenosphere upwelling as well as crustal radioactivity caused LVZs, which can decouple upper and lower crust deformations. Thus, we conclude that the observed fast polarization direction that is consistent with the surface deformation might have mainly formed during the initial

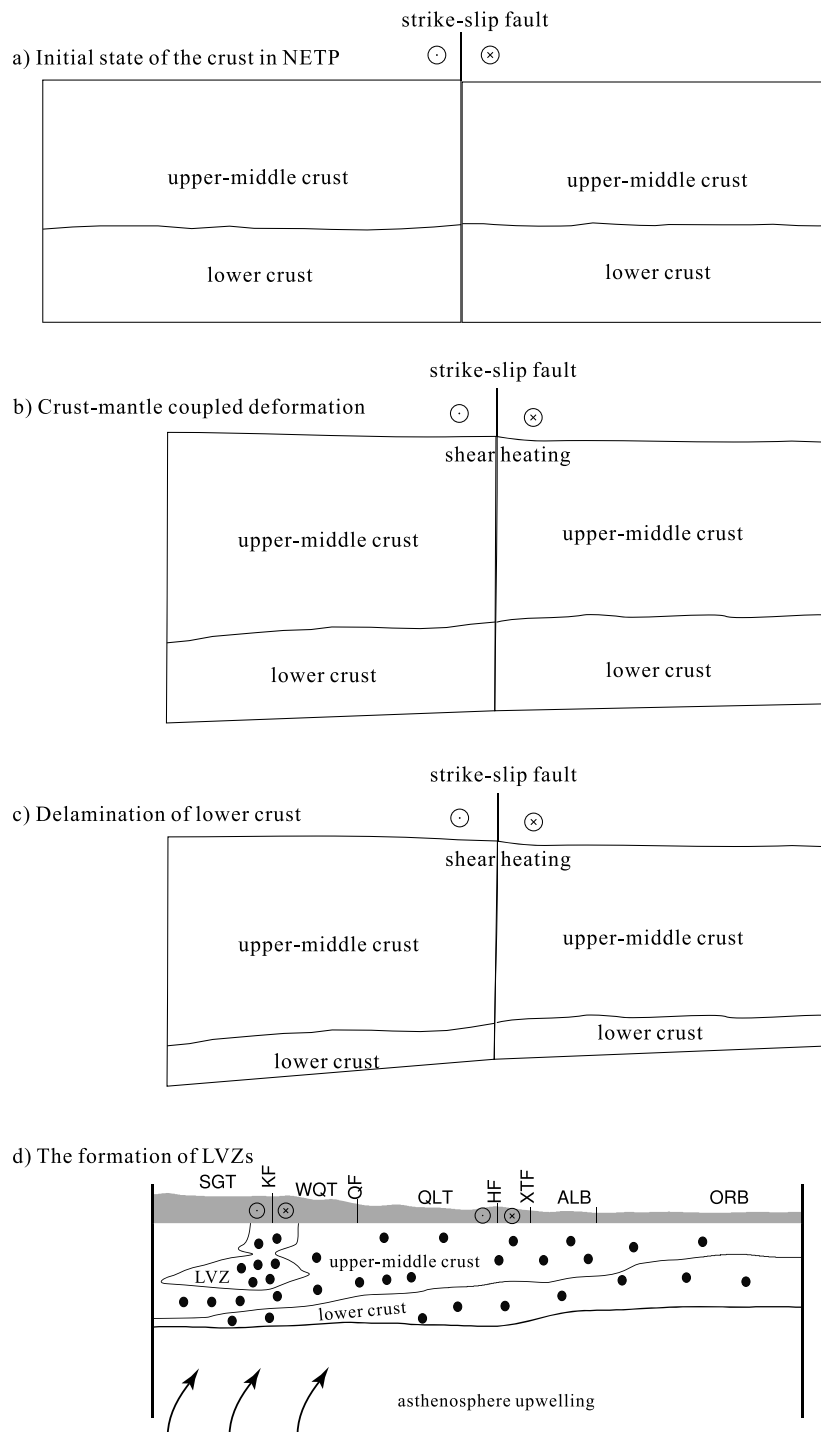


**Figure 10.** Interpretive sketch (not to scale) showing the crustal deformation of the NETP and its adjacent blocks from the initial stage to present. (a) Initial state of the crust beneath the NETP. (b) Crust-mantle coupled deformation. (c) Delamination of the lower crust. (d) The deformation of the crust in present, modified from Figure 9c. The black dots represent the radioactive elements.

stage, although the late formed LVZs may cause decoupled upper-lower crust deformation. This would reconcile the contradiction between the presence of the LVZs and seemingly coherent deformation of the lithosphere. The delamination of lower crust caused the crustal thickening in the NETP concentrated in the upper-middle crust.

From joint analysis, the causes of the crustal thickening and the origins of the LVZs, we therefore further propose that the crustal deformation beneath the NETP is accommodated by a combination of shear motion along strike-slip faults, thickening of the upper and middle crust, and removal of the lower crust (Figure 10). Multiple processes contributed to the crustal deformation in NE Tibet.

### 5.3. Tectonic Processes of the Western NCC

In contrast to compressional deformation in the NETP and Alxa block, the graben basins around the Ordos block are major tectonic features of late Cenozoic extension. The subduction of the Pacific Plate and the collision between the Indian and Asian Plates caused mantle convection beneath the western NCC during the Oligocene [Ren *et al.*, 2002; Tian *et al.*, 2011; Zhang *et al.*, 1998]. A previous geological study indicated that the entire periphery of the Ordos block suffered significant extension after the late Neogene [Zhang *et al.*, 1998]. The YH graben is covered by the thickest sediments, locally up to 10 km in thickness (Figure 6), indicating that this area has suffered more significant subsidence. The depositional thickness decreases southeastward in the Ordos block (Figure 6), suggesting that the extensional effect caused by the mantle convection decreased southeastward [Zhang *et al.*, 1998]. The relatively low velocity in the upper mantle beneath the northern Ordos block (Figures 8g–8h) may represent upwelling of asthenospheric material and may indicate that the northern Ordos block experienced lithospheric modification during the Cenozoic [e.g., Bao *et al.*, 2015a; Wei *et al.*, 2015]. Thus, the modification of the lithosphere beneath the Ordos block may also be associated with the mantle flow. The velocity increases from northwest to southeast in the lower crust and upper mantle beneath the Ordos block (Figures 8d and 8e), implying that the strength of lithospheric modification also decreases southeastward beneath this block.

The Ordos block is traditionally considered to be a cratonic block with an Archean basement [Liu *et al.*, 2006]. However, the crustal thickness of ~46 km beneath the southwestern part (Figure 7) is thicker than the global average of 41.5 km beneath shields and platforms [Christensen and Mooney, 1995], even if we subtract the 1–3 km of sedimentary cover. In addition, the crustal thickness of ~46 km in the southwestern part is also thicker than that in the central part, indicating that the crust in the southwestern Ordos block may have undergone slight thickening. From shear wave splitting results, Yu and Chen [2016] proposed an asthenospheric flow model and suggested that the lithospheric root of the southwestern Ordos block is currently being replaced. The presence of relatively low velocity in the upper mantle [e.g., Li *et al.*, 2017] may be accounted for by the asthenospheric flow under the southwestern Ordos block. Combined with these results, we therefore infer that the crust in southwestern Ordos block has been slightly modified by the eastward asthenospheric flow.

A remarkable contrast in crustal velocity structure is revealed between the Ordos block and the Alxa block (Figures 8c–8e), in association with decreasing gravity anomaly from west to east across the Liupanshan (LPS) thrust belt [Meng *et al.*, 2012]. To the west of the LPS thrust belt in the Ordos block, high *S* wave velocity (3.7–4.0 km/s) is imaged in the middle-lower crust, whereas the Alxa block is characterized by low *S* wave velocity (3.6–3.8 km/s) to the east of the LPS thrust belt. Both sedimentary and crustal thickness also exhibit significant lateral variations across the LPS thrust belt, with thicker sediments and thinner crust in the Ordos block and thinner sediments and thicker crust in the Alxa block. These observations indicate that the LPS thrust belt is the western boundary of the Ordos blocks [Bao *et al.*, 2011; Meng *et al.*, 2012]. The contrasts between the blocks imply different crustal origins for the Alxa and Ordos block and support that the Alxa block is not part of the NCC [e.g., Dan *et al.*, 2016; Wei and Yang, 2015].

Our results provide for the first time a complete picture of the lithospheric structure in considerable detail for the Alxa block. There are significant lateral heterogeneities within the Alxa block. The western part is marked by a thick crust; the eastern part possesses a thin crust (Figure 7). The western Alxa block exhibits a thin lithosphere [Shen *et al.*, 2017] with a low  $V_s$  value in the lithospheric mantle (Figures 7g and 7h); in contrast, thick lithosphere [Shen *et al.*, 2017] with a high velocity (Figures 7g and 7h) in the lithospheric mantle is present beneath the eastern Alxa block and Ordos block. The significant lateral variation in lithospheric structure indicates that the western part may have been modified as a result of the far-field effect of the India-Asia collision, whereas the eastern part appears to have been less influenced.

### 5.4. Implications for Seismogenesis

The Global Positioning System (GPS) velocity field of the study region (Figure 1) changes direction from northeastward to eastward and even to southeastward [Gan *et al.*, 2007]. This pattern indicates that

oblique convergence between the NETP and the Asian Plate has led to slip partitioning with coexisting strike-slip and thrust motions on the HF and NQF. Large earthquakes are generally believed to occur in major fault zones or along boundaries between different tectonic units [Cheng *et al.*, 2016]. A comparison of the hypocentral distribution of large earthquakes with crustal thickness shows that both the Haiyuan and Gulang earthquakes occurred in the major fault zones where there is a sharp transition from thick crust to thin crust (Figure 7). In velocity profiles, the hypocentral regions are characterized by significant lateral heterogeneity (Figures 9b and 9c). In the upper-to-middle crust, the QLT exhibits low  $V_s$ , whereas relatively high  $V_s$  occurs beneath the Alxa block, indicating different crustal mechanical strengths between the QLT and the Alxa block. The India-Asia collision and the later sustained compression have caused the crust to deform continuously within and across blocks, but the deformation has been affected by the strength of the blocks. Thus, localized different deformation between the different blocks can trigger earthquakes as a response to the shearing and thrusting.

To study the seismogenesis further, we used the catalog of earthquakes since 1900 from the *International Seismological Centre* [2014]. Most moderate-to-large earthquakes occurred at depths of 8–15 km in our study area. Thus, earthquakes with a magnitude of  $\geq 5.0$  are displayed at a depth of 12 km (Figure 8b). The lateral resolution of our model is ~40 km, so hypocenters with perpendicular distance less than 40 km are projected to the profiles (Figure 9). In the hypocentral regions of these earthquakes,  $V_s$  displays significant lateral heterogeneity and changes drastically over a short distance in the upper crust, which is consistent with a previous tomographic study in this region [e.g., Cheng *et al.*, 2016]. Importantly, the catalog also shows that 50% of the moderate-to-large earthquakes occurred in the western QLT; the remainder took place in fault zones or along the boundaries between different tectonic units. Thus, we mainly discuss the occurrences of earthquakes in the western QLT. There is an LVZ in the middle crust beneath the western QLT (Figures 8c, 8d, and 9e), so we infer that the observed LVZ in the western QLT may act as an intracrustal decollement decoupling deformation between the upper and lower crust, causing the deformation to vary at different depths. This may be one of the reasons that moderate to strong earthquakes have frequently occurred in this region, although a better understanding of the seismogenesis requires further studies.

## 6. Conclusions

We obtained a new 3-D lithospheric  $S$  wave velocity model for the NETP and western NCC by joint inversion of RFs and Rayleigh wave dispersions. The new model can provide important insights into the geodynamics of the NETP and western NCC. The main findings of this work can be summarized as follows.

1. The NA method was used to determine detailed sedimentary structure by inverting the high-frequency RFs. A thick sedimentary layer is present in the YH graben, Ordos block, and western Alxa block, in good agreement with the results of active-source seismic profiles. The YH graben is covered by thickest sediments, locally up to 10 km in thickness. The sedimentary thickness in the Ordos block decreases from 5–6 km in the west to 3–4 km in the east, with an average thickness of ~4 km.
2. Two crustal LVZs were detected in the NETP. Based on our geophysical data and analyses presented here along with previous studies, we suggest that the LVZ beneath the KF zone may be caused by a combined effect of shear heating, localized asthenosphere upwelling, and crustal radioactivity. The LVZ in the western QLT may represent an early stage of the LVZ that has developed in the northern SGT and southwestern WQT. We further propose that shear motion along the strike-slip fault, thickening of the upper and middle crust, and removal of mafic lower crust played an important role in accommodating the crustal deformation beneath the NETP.
3. The western Alxa block and southwestern Ordos block features a thick crust (~50 and 46 km), whereas the eastern Alxa block and central Ordos block has a thin crust (~45 and 41 km). The lateral variations in the lithospheric structure imply that the southwestern Ordos block and the western Alxa block have been modified.
4. We identify significant contrasts in the  $S$  wave velocity structure of the middle-lower crust between the Ordos block and the Alxa block. The relatively high  $S$  wave velocity (3.7–4.0 km/s) is imaged in the middle-lower crust beneath the Ordos block, whereas the Alxa block is characterized by low  $S$  wave velocity (3.6–3.8 km/s). The contrasts between the blocks support that the Alxa block is not part of the NCC.

5. The LVZ beneath the western QLT can act as an intracrustal decollement to decouple deformation between the upper and lower crust and plays a key role in seismogenesis.

### Acknowledgments

This manuscript benefited from constructive reviews by Walter D. Mooney and an anonymous reviewer. The waveform data were provided by Data Management Center of China National Seismic Network at Institute of Geophysics, China Earthquake Administration, which will be openly available 3 years later after the completion of ChinArray (Phase II) in compliance to the seismic data policy of CEA. This work was supported by the National Science Foundation (NSF) of China (grants 41404069 and 41404074), the China National Special Fund for Earthquake Scientific Research of Public Interest (grant 201308011), the Scientific Institution Basal Research Fund (grant DQJB15A03), NSF of USA (grant EAS-1249701), and the Fundamental Research Funds for the Central Universities. All Figures were produced by using GMT [Wessel *et al.*, 2013].

### References

- Bao, X., M. Xu, L. Wang, N. Mi, D. Yu, and H. Li (2011), Lithospheric structure of the Ordos block and its boundary areas inferred from Rayleigh wave dispersion, *Tectonophysics*, 499(1–4), 132–141.
- Bao, X., X. Song, M. Xu, L. Wang, X. Sun, N. Mi, D. Yu, and H. Li (2013), Crust and upper mantle structure of the North China Craton and the NE Tibetan plateau and its tectonic implications, *Earth Planet. Sci. Lett.*, 369, 129–137.
- Bao, X., D. W. Eaton, and B. Guest (2014), Plateau uplift in western Canada caused by lithospheric delamination along a craton edge, *Nat. Geosci.*, 7(11), 830–833, doi:10.1038/ngeo2270.
- Bao, X., X. Song, and J. Li (2015a), High-resolution lithospheric structure beneath mainland China from ambient noise and earthquake surface-wave tomography, *Earth Planet. Sci. Lett.*, 417, 132–141.
- Bao, X., et al. (2015b), Two crustal low-velocity channels beneath SE Tibet revealed by joint inversion of Rayleigh wave dispersion and receiver functions, *Earth Planet. Sci. Lett.*, 415, 16–24.
- Bendick, R., and L. Flesch (2007), Reconciling lithospheric deformation and lower crustal flow beneath central Tibet, *Geology*, 35, 895–898.
- Berteussen, K. A. (1977), Moho depth determinations based on spectral-ratio analysis of NORSAR long-period P waves, *Phys. Earth Planet. Inter.*, 31(1), 13–27.
- Chang, L., C. Wang, and Z. Ding (2011), Upper mantle anisotropy in the Ordos block and its margins, *Sci. China Earth Sci.*, 54(6), 888–900.
- Chang, L., Z. Ding, C. Wang, and L. M. Flesch (2017), Vertical coherence of deformation in lithosphere in the NE margin of the Tibetan Plateau using GPS and shear-wave splitting data, *Tectonophysics*, 699, 93–101.
- Chen, L. (2010), Concordant structural variations from the surface to the base of the upper mantle in the North China Craton and its tectonic implications, *Lithos*, 120(1–2), 96–115.
- Chen, L., M. Jiang, J. Yang, Z. Wei, C. Liu, and Y. Ling (2014), Presence of an intralithospheric discontinuity in the central and western North China Craton: Implications for destruction of the craton, *Geology*, 42(3), 223–226.
- Cheng, B., D. Zhao, S. Cheng, Z. Ding, and G. Zhang (2016), Seismic tomography and anisotropy of the Helan-Liupan tectonic belt: Insight into lower crustal flow and seismotectonics, *J. Geophys. Res. Solid Earth*, 121, 2608–2635, doi:10.1002/2015JB012692.
- ChinArray-Himalaya (2011), *China Seismic Array Waveform Data of Himalaya Project*, Institute of Geophysics, China Earthquake Administration, Beijing.
- Christensen, N. I., and W. D. Mooney (1995), Seismic velocity structure and composition of the continental crust: A global view, *J. Geophys. Res.*, 100, 9761–9788, doi:10.1029/95JB00259.
- Chung, S. L., M. F. Chu, Y. Zhang, Y. Xie, C. H. Lo, T. Y. Lee, X. Li, Q. Zhang, and Y. Wang (2005), Tibetan tectonic evolution inferred from spatial and temporal variations in post-collisional magmatism, *Earth Sci. Rev.*, 68(3), 173–196.
- Clark, M. K., and L. H. Royden (2000), Topographic ooze: Building the eastern margin of Tibet by lower crustal flow, *Geology*, 28(8), 703.
- Dan, W., X.-H. Li, Q. Wang, X.-C. Wang, D. A. Wyman, and Y. Liu (2016), Phanerozoic amalgamation of the Alxa Block and North China Craton: Evidence from Paleozoic granitoids, U-Pb geochronology and Sr-Nd-Pb-Hf-O isotope geochemistry, *Gondwana Res.*, 32, 105–121.
- England, P., and G. Houseman (1986), Finite strain calculations of continental deformation: 2. Comparison with the India-Asia collision zone, *J. Geophys. Res.*, 91, 3664–3676, doi:10.1029/JB091iB03p03664.
- England, P., and D. McKenzie (1982), A thin viscous sheet model for continental deformation, *Geophys. J. Int.*, 70(2), 295–321.
- Feng, S. Y., R. Gao, C. X. Long, S. M. Fang, C. B. Zhao, K. P. Kou, Y. L. Tan, and H. Y. He (2011), The compressive stress field of Yinchuan garben: Deep seismic reflection profile (in Chinese with English abstract), *Chin. J. Geophys.*, 54(3), 692–697.
- Flesch, L., W. Holt, P. Silver, M. Stephenson, C. Wang, and W. Chan (2005), Constraining the extent of crust-mantle coupling in central Asia using GPS, geologic, and shear wave splitting data, *Earth Planet. Sci. Lett.*, 238, 248–268.
- Gan, W., P. Zhang, Z. Shen, Z. Niu, M. Wang, Y. Wan, D. Zhou, and J. Cheng (2007), Present-day crustal motion within the Tibetan Plateau inferred from GPS measurements, *J. Geophys. Res.*, 112, B08416, doi:10.1029/2005JB004120.
- Gao, S., B. R. Zhang, T. C. Luo, Z. J. Li, Q. L. Xie, X. M. Gu, H. F. Zhang, J. P. Ouyang, D. P. Wang, and C. L. Gao (1992), Chemical composition of the continental crust in the Qinling Orogenic Belt and its adjacent North China and Yangtze cratons, *Geochim. Cosmochim. Acta*, 56(11), 3933–3950.
- Gong, J., J. Zhang, Z. Wang, S. Yu, H. Li, and Y. Li (2015), Origin of the Alxa Block, western China: New evidence from zircon U-Pb geochronology and Hf isotopes of the Longshoushan Complex, *Gondwana Res.*, 36, 359–375.
- Guo, W., S. Jia, Y. Duan, and F. Wang (2016), A study on the basement tectonic units in the northeast margin of Tibetan Plateau—The result of Maduo-Gonghe-Yabrai refraction profile [in Chinese with English abstract], *Chin. J. Geophys.*, 59(10), 3627–3636, doi:10.6038/cjg20161010.
- Guo, Z., and Y. J. Chen (2016), Crustal structure of the eastern Qinling orogenic belt and implication for reactivation since the Cretaceous, *Tectonophysics*, 683, 1–11.
- Guo, Z., and Y. J. Chen (2017), Mountain building at northeastern boundary of Tibetan Plateau and craton reworking at Ordos block from joint inversion of ambient noise tomography and receiver functions, *Earth Planet. Sci. Lett.*, v, 232–242.
- Hacker, B. R., E. Gnos, L. Ratschbacher, M. Grove, M. McWilliams, S. V. Sobolev, J. Wan, and W. Zhenhan (2000), Hot and dry deep crustal xenoliths from Tibet, *Science*, 287, 2463–2466.
- Harley, S. L. (1989), The origins of granulites: A metamorphic perspective, *Geol. Mag.*, 126, 215–247.
- Harley, S. L. (2004), Extending our understanding of ultrahigh temperature crustal metamorphism, *J. Mineral. Petrol. Sci.*, 99, 140–158 (Special Issue).
- Herrmann, R. B. (2013), Computer programs in seismology: An evolving tool for instruction and research, *Seismol. Res. Lett.*, 84(6), 1081–1088.
- Hu, S., L. He, and J. Wang (2000), Heat flow in the continental area of China: A new data set, *Earth Planet. Sci. Lett.*, 179(2), 407–419.
- International Seismological Center (2014), *On-line Bulletin*, Internatl. Seismol. Cent., Thatcham, U. K. [Available at <http://www.isc.ac.uk/>.]
- Jia, S., X. Zhang, J. Zhao, F. Wang, C. Zhang, Z. Xu, J. Pan, Z. Liu, S. Pan, and G. Sun (2010), Deep seismic sounding data reveal the crustal structures beneath Zoigé basin and its surrounding folded orogenic belts, *Sci. China Earth Sci.*, 53, 203–212.
- Jiang, C., Y. Yang, and Y. Zheng (2014), Penetration of mid-crustal low velocity zone across the Kunlun fault in the NE Tibetan Plateau revealed by ambient noise tomography, *Earth Planet. Sci. Lett.*, 406(3), 369–382.
- Julià, J., C. J. Ammon, R. B. Herrmann, and A. M. Correig (2000), Joint inversion of receiver function and surface wave dispersion observations, *Geophys. J. Int.*, 143(1), 99–112.

- Julià, J., C. J. Ammon, and A. A. Nyblade (2005), Evidence for mafic lower crust in Tanzania, East Africa, from joint inversion of receiver functions and Rayleigh wave dispersion velocities, *Geophys. J. Int.*, 162(2), 555–569.
- Leloup, P. H., Y. Ricard, J. Battaglia, and R. Lacassin (1999), Shear heating in continental strike-slip shear zones: Model and field examples, *Geophys. J. Int.*, 136(1), 19–40.
- Li, H., Y. Shen, Z. Huang, X. Li, M. Gong, D. Shi, E. Sandvol, and A. Li (2014), The distribution of the mid-to-lower crustal low-velocity zone beneath the northeastern Tibetan Plateau revealed from ambient noise tomography, *J. Geophys. Res. Solid Earth*, 119, 1954–1970, doi:10.1002/2013JB010374.
- Li, J., X. Wang, and F. Niu (2011), Seismic anisotropy and implications for mantle deformation beneath the NE margin of the Tibet Plateau and Ordos Plateau, *Phys. Earth Planet. Inter.*, 189, 157–170.
- Li, L., A. Li, Y. Shen, E. A. Sandvol, D. Shi, H. Li, and X. Li (2013), Shear wave structure in the northeastern Tibetan Plateau from Rayleigh wave tomography, *J. Geophys. Res. Solid Earth*, 118, 4170–4183, doi:10.1002/jgrb.50292.
- Li, L., A. Li, M. A. Murphy, and Y. V. Fu (2016), Radial anisotropy beneath northeast Tibet, implications for lithosphere deformation at a restraining bend in the Kunlun fault and its vicinity, *Geochem. Geophys. Geosyst.*, 17, 3674–3690, doi:10.1002/2016GC006366.
- Li, X., M. Santosh, S. Cheng, X. Xu, and W. Zhong (2015), Crustal structure and composition beneath the northeastern Tibetan Plateau from receiver function analysis, *Phys. Earth Planet. Inter.*, 249, 51–58.
- Li, Y., Q. Wu, Z. An, X. Tian, R. Zeng, R. Zhang, and H. Li (2006), The Poisson's ratio and crustal structure across the NE Tibetan Plateau determined from receiver functions [in Chinese with English abstract], *Chin. J. Geophys.*, 49(5), 1359–1368.
- Li, Y., J. Pan, Q. Wu, and Z. Ding (2017), Lithospheric structure beneath the northeastern Tibetan Plateau and the western Sino-Korea craton revealed by Rayleigh-wave tomography, *Geophys. J. Int.*, 210(2), 570–584, doi:10.1093/gji/ggx181.
- Liang, S., W. Gan, C. Shen, G. Xiao, J. Liu, W. Chen, X. Ding, and D. Zhou (2013), Three-dimensional velocity field of present-day crustal motion of the Tibetan Plateau derived from GPS measurements, *J. Geophys. Res. Solid Earth*, 118, 5722–5732, doi:10.1002/2013JB010503.
- Ligorra, J. P., and C. J. Ammon (1999), Iterative deconvolution and receiver-function estimation, *Bull. Seismol. Soc. Am.*, 89(5), 1395–1400.
- Liu, M., W. D. Mooney, S. Li, N. Okaya, and S. Detwiler (2006), Crustal structure of the northeastern margin of the Tibetan Plateau from the Songpan-Ganzi terrane to the Ordos basin, *Tectonophysics*, 420(1–2), 253–266.
- McKenzie, D., and K. Priestley (2008), The influence of lithospheric thickness variations on continental evolution, *Lithos*, 102(1), 1–11.
- Meng, X. H., L. Shi, L. H. Guo, T. Tong, and S. Zhang (2012), Multi-scale analyses of transverse structures based on gravity anomalies in the northeastern margin of the Tibetan Plateau [in Chinese with English abstract], *Chin. J. Geophys.*, 55(12), 3933–3941.
- Nie, Z. S., R. Yun, Z. M. Liu, D. U. Cheng-Long, and P. L. Cong (2011), Preliminary study on seismic active faults of the Daqingshan frontal fault in Baotou City, Inner Mongolia (in Chinese with English abstract), *Geoscience*, 25(5), 938–957.
- Pan, S., and F. Niu (2011), Large contrasts in crustal structure and composition between the Ordos Plateau and the NE Tibetan Plateau from receiver function analysis, *Earth Planet. Sci. Lett.*, 303, 291–298.
- Ren, J., K. Tamaki, S. Li, and J. Zhang (2002), Late Mesozoic and Cenozoic rifting and their dynamic setting in eastern China, *Tectonophysics*, 344(3–4), 175–203.
- Royden, L. H., B. C. Burchfiel, R. W. King, E. Wang, Z. Chen, F. Shen, and Y. Liu (1997), Surface deformation and lower crustal flow in eastern Tibet, *Science*, 276(5313), 788–790.
- Sambridge, M. (1999), Geophysical inversion with a neighbourhood algorithm—I. Searching a parameter space, *Geophys. J. Int.*, 138(2), 479–494.
- Shen, X., M. Liu, Y. Gao, W. Wang, Y. Shi, M. An, Y. Zhang, and X. Liu (2017), Lithospheric structure across the northeastern margin of the Tibetan Plateau: Implications for the plateau's lateral growth, *Earth Planet. Sci. Lett.*, 459, 80–92.
- Srinivas, D., D. Srinagesh, R. K. Chadha, and M. Ravi Kumar (2013), Sedimentary thickness variations in the Indo-Gangetic Foredeep from inversion of receiver functions, *Bull. Seismol. Soc. Am.*, 103(4), 2257–2265.
- Tapponnier, P., and P. Molnar (1976), Slip-line field theory and large-scale continental tectonics, *Nature*, 264(25), 319–324.
- Tapponnier, P., G. Peltzer, A. Y. Dain, and R. Armijo (1982), Propagating extrusion tectonics in Asia: New insights from simple experiments with plasticine, *Geology*, 10, 611–616.
- Teng, J., Z. Zhang, X. Zhang, C. Wang, R. Gao, B. Yang, Y. Qiao, and Y. Deng (2013), Investigation of the Moho discontinuity beneath the Chinese mainland using deep seismic sounding profiles, *Tectonophysics*, 609, 202–216.
- Teng, J., S. Li, Y. Zhang, J. Zhao, J. Pi, F. Wang, Y. Yan, H. Yang, G. Hu, and S. Pan (2014), Seismic wave fields and dynamical response for Qinling orogen and sedimentary basins and crystalline basement [in Chinese with English abstract], *Chin. J. Geophys.*, 57(3), 770–788, doi:10.6038/cjg20140308.
- Tian, X., and Z. Zhang (2013), Bulk crustal properties in NE Tibet and their implications for deformation model, *Gondwana Res.*, 24, 548–559.
- Tian, X., J. Teng, H. Zhang, Z. Zhang, Y. Zhang, H. Yang, and K. Zhang (2011), Structure of crust and upper mantle beneath the Ordos Block and the Yinshan Mountains revealed by receiver function analysis, *Phys. Earth Planet. Inter.*, 184(3), 186–193.
- Tian, X., Z. Liu, S. Si, and Z. Zhang (2014), The crustal thickness of NE Tibet and its implication for crustal shortening, *Tectonophysics*, 634, 198–207.
- Vergne, J., G. Wittlinger, Q. Hui, P. Tapponnier, G. Poupinet, J. Mei, G. Herquel, and A. Paul (2002), Seismic evidence for stepwise thickening of the crust across the NE Tibetan Plateau, *Earth Planet. Sci. Lett.*, 203(1), 25–33.
- Wang, C. Y., L. M. Flesch, P. G. Silver, L. J. Chang, and W. W. Chan (2008), Evidence for mechanically coupled lithosphere in central Asia and resulting implications, *Geology*, 36(5), 363–366.
- Wang, C. Y., E. Sandvol, L. Zhu, H. Lou, Z. Yao, and X. Luo (2014), Lateral variation of crustal structure in the Ordos block and surrounding regions, North China, and its tectonic implications, *Earth Planet. Sci. Lett.*, 387, 198–211.
- Wang, H., R. Gao, L. Zeng, Z. Kuang, A. Xue, W. Li, X. Xiong, and W. Huang (2014), Crustal structure and Moho geometry of the northeastern Tibetan plateau as revealed by SinoProbe-02 deep seismic-reflection profiling, *Tectonophysics*, 636(1), 32–39.
- Wang, P., et al. (2013), Seismic evidence for the stratified lithosphere in the south of the North China Craton, *J. Geophys. Res. Solid Earth*, 118, 570–582, doi:10.1029/2011JB008946.
- Wang, Q., F. Niu, Y. Gao, and Y. Chen (2016), Crustal structure and deformation beneath the NE margin of the Tibetan Plateau constrained by teleseismic receiver function data, *Geophys. J. Int.*, 204(1), 167–179.
- Wang, S. J., F. Y. Wang, F. S. Zhang, S. X. Jia, C. K. Zhang, J. R. Zhao, and B. F. Liu (2014), The P-wave velocity structure of the lithosphere of the North China Craton—Results from the Wendeng-Alxa Left Banner deep seismic sounding profile, *Sci. China Earth Sci.*, 57, 2053–2063.
- Wang, W., J. Wu, L. Fang, G. Lai, and Y. Cai (2017), Sedimentary and crustal thicknesses and Poisson's ratios for the NE Tibetan Plateau and its adjacent regions based on dense seismic arrays, *Earth Planet. Sci. Lett.*, 462, 76–85.
- Wang, X., Z. Ding, L. Zhu, and Y. Wu (2017), Crustal thicknesses and Poisson's ratios beneath the northern section of the north-south seismic belt and its surrounding area in China [in Chinese with English abstract], *Chin. J. Geophys.*, 60(6), 2080–2090, doi:10.6038/cjg20170605.

- Wei, Y., and Z. Yang (2015), The Alashan Terrane was not part of North China by the Late Devonian: Evidence from detrital zircon U-Pb geochronology and Hf isotopes, *Gondwana Res.*, 27(3), 1270–1282.
- Wei, Z., L. Chen, M. Jiang, and Y. Ling (2015), Lithospheric structure beneath the central and western North China Craton and the adjacent Qilian orogenic belt from Rayleigh wave dispersion analysis, *Tectonophysics*, 646, 130–140.
- Wessel, P., W. H. F. Smith, R. Scharroo, J. Luis, and F. Wobbe (2013), Generic mapping tools: Improved version released, *Eos Trans. AGU*, 94(45), 409–410.
- Xiao, Q., J. Zhang, G. Zhao, and J. Wang (2013), Electrical resistivity structures northeast of the Eastern Kunlun Fault in the Northeastern Tibet: Tectonic implications, *Tectonophysics*, 601, 125–138.
- Xiao, Q., G. Shao, G. Yu, J. Cai, and J. Wang (2016), Electrical resistivity structures of the Kunlun-Qaidam-Qilian system at the northern Tibet and their tectonic implications, *Phys. Earth Planet. Inter.*, 255, 1–17.
- Xu, T., Z. Wu, Z. Zhang, X. Tian, Y. Deng, C. Wu, and J. Teng (2014), Crustal structure across the Kunlun fault from passive source seismic profiling in East Tibet, *Tectonophysics*, 627, 98–107.
- Yang, Y., M. H. Ritzwoller, Y. Zheng, W. Shen, A. L. Levshin, and Z. Xie (2012), A synoptic view of the distribution and connectivity of the mid-crustal low velocity zone beneath Tibet, *J. Geophys. Res.*, 117, B04303, doi:10.1029/2011JB008810.
- Yin, A., and T. M. Harrison (2000), Geologic evolution of the Himalayan-Tibetan orogen, *Annu. Rev. Earth Planet. Sci.*, 28, 211–280.
- Yu, Y., and Y. J. Chen (2016), Seismic anisotropy beneath the southern Ordos block and the Qinling-Dabie orogen, China: Eastward Tibetan asthenospheric flow around the southern Ordos, *Earth Planet. Sci. Lett.*, 455, 1–6.
- Zhan, Y., G. Z. Zhao, L. F. Wang, J. J. Wang, X. Chen, L. Q. Zhao, Q. B. X. (2014), Deep electric structure beneath the intersection area of West Qinling orogenic zone with north-south seismic tectonic zone in China [in Chinese with English abstract], *Chin. J. Geophys.*, 57(8), 2594–2607, doi:10.6038/cjg20140819.
- Zhang, H., J. Teng, X. Tian, Z. Zhang, R. Gao, and J. Liu (2012), Lithospheric thickness and upper-mantle deformation beneath the NE Tibetan Plateau inferred from S receiver functions and SKS, splitting measurements, *Geophys. J. Int.*, 191(3), 1285–1294.
- Zhang, H. S., R. Gao, X. B. Tian, J. W. Teng, Q. S. Li, Z. Ye, Z. Liu, and S. K. Si (2015), Crustal S-wave velocity beneath the northeastern Tibetan Plateau inferred from teleseismic P-wave receiver functions [in Chinese with English abstract], *Chin. J. Geophys.*, 58(11), 3982–3992.
- Zhang, Q., E. Sandvol, J. Ni, Y. Yang, and Y. Chen (2011), Rayleigh wave tomography of the northeastern margin of the Tibetan Plateau, *Earth Planet. Sci. Lett.*, 304, 103–112.
- Zhang, Y. Q., J. L. Mercier, and P. Vergly (1998), Extension in the rift systems around the Ordos (China), and its contribution to the extrusion tectonics of south China with respect to Gobi-Mongolia, *Tectonophysics*, 285(1), 41–75.
- Zhang, Z., Z. Bai, S. Klemperer, X. Tian, T. Xu, Y. Chen, and J. Teng (2013), Crustal structure across northeastern Tibet from wide-angle seismic profiling: Constraints on the Caledonian Qilian orogeny and its reactivation, *Tectonophysics*, 606, 140–159.
- Zhao, L. Q., Y. Zhan, X. B. Chen, H. Yang, and F. Jiang (2015), Deep electrical structure of the central West Qinling orogenic belt and blocks on its either side [in Chinese with English abstract], *Chin. J. Geophys.*, 58(7), 2460–2472.
- Zheng, D., H. Li, Y. Shen, J. Tan, L. Ouyang, and X. Li (2016), Crustal and upper mantle structure beneath the northeastern Tibetan Plateau from joint analysis of receiver functions and Rayleigh wave dispersions, *Geophys. J. Int.*, 204(1), 583–590.